第45卷第3期
2026年6月

红外与毫米波学报
Journal of Infrared and Millimeter Waves

Vol. 45, No. 3
June, 2026

文章编号：1001-9014(2026)03-0357-09

DOI: 10.11972/j.issn.1001-9014.2026.03.002

Terahertz detector based on side-gate AlGaN/GaN HEMT for resonant detection

Jin Chen-Yang[1,3,4,5], Kang Ya-Ru[1,5], Li Ye-Ran[1,3,6], Yan Wei[1,3*], Ning Jin[1,3,4,5], Zhao Yong-Mei[1,3,4,5], Li Zhao-Feng[1,2,3,4,5*], Yang Fu-Hua[1,2,3], Wang Xiao-Dong[1,2,3,5]

(1. Engineering Research Center for Semiconductor Integrated Technology, Institute of Semiconductors, Chinese Academy of Sciences, Beijing 100083, China
2. Center of Materials Science and Optoelectronics Engineering, University of Chinese Academy of Sciences, Beijing 100049, China
3. College of Materials Science and Opto-Electronics Technology, University of Chinese Academy of Sciences, Beijing 100049, China
4. School of Electronic, Electrical and Communication Engineering, University of Chinese Academy of Sciences, Beijing 100049, China
5. School of Integrated Circuits, University of Chinese Academy of Sciences, Beijing 100049, China;
6. Huairou Laboratory, Beijing 101499, China)

Abstract: In high-electron-mobility transistor (HEMT) terahertz detectors, an excessively wide gate can generate oblique modes in the channel, resulting in weakened resonant detection signals and a broadened resonance peak. To address this issue, a side-gate HEMT (EdgeFET) structure was proposed. A resonant detection model for the side-gate device was established based on the hydrodynamic equations of the two-dimensional electron gas (2DEG) in conventional HEMT. A side-gate HEMT detector was fabricated, and terahertz resonant detection experiments were conducted at 77 K. The experimental results indicated that EdgeFET demonstrated distinct resonant responses at 77 K, with the resonant responsivity reaching 3.7 times the maximum non-resonant responsivity. The experimental data were fitted using the theoretical model to validate its accuracy. These results strongly confirm the effectiveness of EdgeFET in enhancing the resonant performance of the detector, providing a new technological approach for the development of next-generation high-performance terahertz detectors.

Key words: AlGaN/GaN HEMT, side-gate, terahertz, resonant detection

Introduction

Due to its substantial potential in various applications, such as medical imaging, high-speed communications, radar, security screening, and non-destructive testing, THz detection technology has garnered significant attention. [1-4] Compared to other THz detectors, high electron mobility transistor (HEMT) THz detectors have been extensively studied over the past few decades due to their advantages, including low noise-equivalent power (NEP), high responsivity (R_v), fast response time, simple structure, and ease of fabrication and integration. [5-8]

In the early 1990s, Dyakonov and Shur indicated that a field-effect transistor (FET) channel could serve as a resonant cavity for plasma waves. [9] Carrier movement can resemble shallow water waves when the carrier mobility in the FET channel is high enough to minimize collisions with protons or impurities during transit, constructing a plasma wave whose oscillation frequency is controlled by the gate. As the channel length is reduced to a submicron scale, the plasma wave reflects at the device boundary, causing carrier motion instability and frequency oscillations in the terahertz band. Specific boundary conditions can create a steady photoresponse current or voltage between the source and drain when the frequency of an incident THz wave matches or exceeds that of the plasma wave, enabling THz radiation detection. This theory clarifies the relationship between response voltage, gate length, operating temperature, and oscillation frequency.

Received date: 2025-03-26, **accepted date**: 2025-04-28, 收稿日期：2025-03-26，录用日期：2025-04-28

Foundation items: Supported by the Strategic Priority Research Program of Chinese Academy of Sciences (XDB43020502); CAS Project for Young Scientists in Basic Research (YSBR-064).

Biography: JIN Chen-Yang (2000-), male, Linfen, master. Research area involves GaN HEMT terahertz detector. E-mail: jinchenyang@semi.ac.cn.

* **Corresponding author**: E-mail: yanwei@semi.ac.cn, lizhaofeng@semi.ac.cn

The FET detector has non-resonant and resonant operating modes. If $\omega\tau \ll 1$ (where ω is the fundamental plasma oscillation frequency and τ is the momentum relaxation time), the FET can operate as a non-resonant detector. The non-resonant detection response is independent of the incident frequency, making it a broadband detection mechanism[10-11]. If $\omega\tau \gg 1$, the FET can operate as a resonant detector. Plasma oscillations with a high-quality factor may be excited in the FET channel. The resonant response will be much greater than the non-resonant response[12]. Resonant detection exhibits frequency selectivity that occurs when the incident wave frequency matches the fundamental or odd multiples of the intrinsic plasma wave frequency[9]. The plasma wave's oscillation frequency can be obtained as[10]

$$f = \frac{\omega_0}{2\pi} = \frac{s}{4L} = \frac{1}{4L}\sqrt{\frac{q\left(V_g - V_{th}\right)}{m}} \quad , \quad (1)$$

where s is the plasma wave velocity; L is the gate length; m is the effective electron mass; q is the electron charge; V_g and V_{th} are the gate and threshold voltages, respectively.

Although resonant responses were observed experimentally, high-quality-factor resonant was not achieved[13-17], primarily due to the fact that the gate width of the FET is much larger than its gate length, which gives rise to oblique plasma wave modes in the channel[18-19].

It is crucial to reduce the gate width to minimize oblique modes. Physical etching has been employed as the primary technique for narrowing the gate width. However, the reduction in gate width is constrained and remains comparable to the gate length in magnitude due to technological limitations. Additionally, physical etching increases surface roughness, enhancing surface scattering, reducing carrier mobility, and decreasing both momentum relaxation time and mass factors that impede effective resonance detection.

Cywinski and Yahniuk constructed a GaN/AlGaN FET with two side-gates (EdgeFET) to enhance resonant performance[20]. Fig. 1 shows the structural diagram and sectional view of the EdgeFET. This design places the gate on both channel sides without metal covering the top. Theoretically, a one-dimensional conductive channel is constructed, eliminating oblique modes and enhancing resonance performance[21].

Unlike traditional JFET with metal-semiconductor contacts, or conventional HEMT, the energy band diagram shown in Fig. 2(a) indicates that the EdgeFET gate has a Schottky contact between metal and 2DEG. This double-gate design laterally compresses the channel width from both sides. Traditional DC transport models for metal-semiconductor contacts in JFET and HEMT no longer apply to EdgeFET, making equation (1), which is based on the asymptotic channel approximation, invalid. A new DC transport model is established for EdgeFET, and preliminary validation is conducted.[22]

Based on the fundamental principles of metal-2DEG Schottky contact, a THz resonance detection response model is established for the EdgeFET THz detector. A GaN/AlGaN EdgeFET THz detector was fabricated with a gate length of 170 nm and a gate width of 200 nm, with a bowtie antenna. The detector is characterized at 77 K using a Backward-Wave Oscillator (BWO) over the frequency range varying from 200 GHz to 384 GHz.

1 The model of terahertz resonant detection for EdgeFET

The hydrodynamics equations of 2DEG in the channel of a traditional HEMT are described by the equation of motion (the Euler equation) and the continuity equation as follows[9]:

$$\frac{\partial v}{\partial t} + v\frac{\partial v}{\partial x} = -\frac{q}{m_n}\frac{\partial U}{\partial x} \quad , \quad (2)$$

$$\frac{\partial \rho}{\partial t} + \frac{\partial\left(\rho v\right)}{\partial x} = 0 \quad , \quad (3)$$

where $U = U_0 + U_a\cos(\omega t - kx)$, is a function of x and t (where $U_0 = U_{gc} - U_{th}$, U_{gc} is the dc gate-to-channel voltage swing, U_{th} is the threshold voltage, $U_a\cos(\omega t - kx)$ is the external ac voltage induced between the gate and channel by the incoming electromagnetic wave, ω and k are the angular frequency and wave number of the plasma

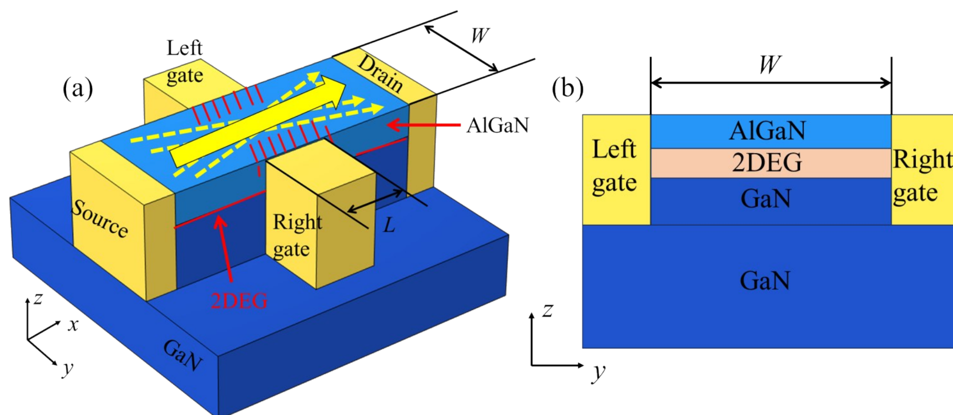

Fig. 1 (a) Structural diagram and (b) Sectional view of the EdgeFET
图1 EdgeFET的结构示意图和剖面图

wave). $\partial U/\partial x$ is the longitudinal electric field in the channel, v is the electron velocity, and m_n is the effective electron mass. $\rho = qn_e$ is the channel's 2DEG surface charge density, where n_e is the electron surface density of the 2DEG. For the traditional HEMT, based on the gradual channel approximation, $\rho = CU$, where C is the gate capacitance per unit area. While for the EdgeFET, the relation between ρ and the gate voltage is deduced in the following.

For the EdgeFET, it is assumed that the gate voltage adjusts the effective channel width, creating a one-dimensional conductive channel containing 2DEG at its center, while the other regions become depletion zones. Therefore, we only focus on the channel center's potential distribution and charge concentration.

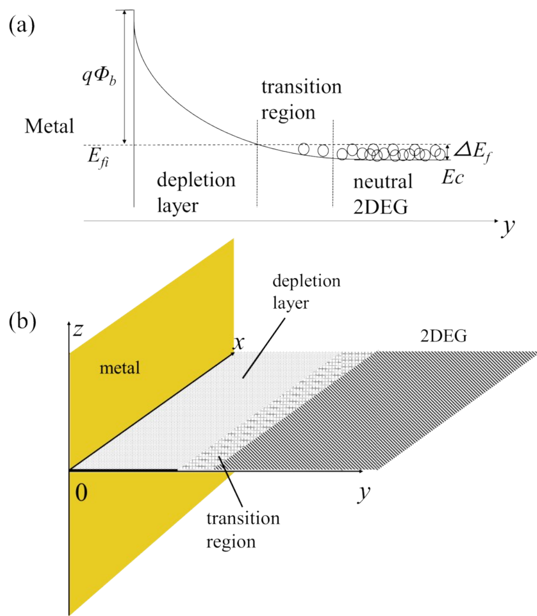

Fig. 2 (a) Energy band diagram of the metal-2DEG contact (E_{fi} is the quasi-Fermi level, E_c is the conduction band minimum, $\Delta E_f = E_{fi}$-E_c, $q\Phi_b$ is the metal-2DEG barrier height); (b) Simplified model of the metal-2DEG contact
图 2 (a)金属-2DEG接触的能带图(Efi是准费米能级,Ec是导带底,ΔEf = Efi-Ec,qΦb是金属-2DEG接触势垒高度);(b)金属-2DEG接触的简化模型

First, the configuration of a unilateral contact between metal and a two-dimensional electron gas (2DEG) is examined, as illustrated in Fig. 2(b). The band bending occurs when a voltage V is applied to the metal ($V = V_0 + V_a\cos(\omega t - kx)$, where V_0 is the dc voltage, $V_a\cos(\omega t - kx)$ is the external ac voltage induced by the incoming THz wave), fully depleting the 2DEG on the metal-adjacent side and constructing a depletion region. In regions distant from the metal gate, the band bending is relatively weak, resulting in the presence of a transition region between the depletion layer and the neutral 2DEG, as illustrated in Fig. 2(a). The width of this transition region is on the order of several effective Bohr radius (The length of the effective Bohr radius is estimated to be several nanometers)[23]. The carriers in the transition region are not completely depleted as in the depletion layer, yet their concentration is lower than that in the neutral region. The potential distribution of the transition region can be described as[23]:

$$\varphi(x,y,0) = \frac{Va_B}{\pi y} \quad , \quad (4)$$

where

$$a_B = \frac{4\pi\hbar^2\varepsilon}{q^2 m_n} \quad , \quad (5)$$

is the effective Bohr radius. ε is the dielectric permittivity; $\hbar$ is the Planck constant.

In EdgeFET gates, the metal configuration changes from unilateral to bilateral. The distance between the two metal gates, denoted by W, determines the channel width. When a voltage V is applied simultaneously to both gates, the potential at the center of the channel can be obtained from Equation (4) as follows:

$$\varphi_0 = 2\varphi\left(x, \frac{W}{2}, 0\right) = \frac{4a_B V}{\pi W} \quad , \quad (6)$$

The intrinsic electron surface density $n_{s,0}$ for a degenerate 2DEG in a heterojunction can be calculated as follows[23]

$$n_{s,0} = \frac{m_n \Delta E_f}{\pi\hbar^2} \quad , \quad (7)$$

ΔE_f represents the difference between the quasi-Fermi level of electrons in the 2DEG and the lowest quantum state within the quantum well containing the 2DEG, as shown in Fig. 2(a).

The electron surface density n_s at the channel center after applying a gate voltage V is[24]

$$n_s = n_{s,0}\left(1 + \frac{q\varphi_0}{\Delta E_f}\right) \quad , \quad (8)$$

$$= n_{s,0} + \frac{16\varepsilon V}{\pi q W} \quad , \quad (9)$$

By analogy with Equation (2), the Euler equation for the 2DEG at the center of the channel in the EdgeFET can be derived as follows (where the U is replaced by φ_0):

$$\frac{\partial v}{\partial t} + v\frac{\partial v}{\partial x} = -\frac{q}{m_n}\frac{\partial \varphi_0}{\partial x} \quad , \quad (10)$$

Hence, by substituting Equation (8) into Equation (10) and using the relation $\rho = qn_s$, the following expression can be obtained:

$$\frac{\partial v}{\partial t} + v\frac{\partial v}{\partial x} = -\frac{\Delta E_f}{m_n n_{s,0}}\frac{\partial n_s}{\partial x} = -\frac{\Delta E_f}{q m_n n_{s,0}}\frac{\partial \rho}{\partial x} \quad , \quad (11)$$

Equations (3) and (11) are the hydrodynamic equations for the EdgeFET, resembling those for the traditional HEMT. By analogy[10], the 2DEG plasma's wave velocity, denoted by s $(=\omega/k)$, can be calculated as

$$s = \sqrt{\frac{\Delta E_f \rho}{q m_n n_{s,0}}} = \sqrt{\frac{\pi\hbar^2}{q m_n^2}\left(q n_{s,0} + \frac{16\varepsilon V}{\pi W}\right)} \quad , \quad (12)$$

The second step of the above equation has used Equations (7) and (9), and the relation $\rho = qn_s$. The required frequency for generating the intrinsic plasma wave, denoted by $f = s/4L$[10], can be expressed as

$$f = \frac{s}{4L} = \frac{1}{4L}\sqrt{\frac{\pi\hbar^2}{qm_n^{\ 2}}\left(qn_{s,0} + \frac{16\varepsilon V}{\pi W}\right)} \quad , \quad (13)$$

A comparison between equations (1) and (13) shows that the intrinsic plasma wave oscillation frequencies between the traditional HEMT and the EdgeFET are considerably different, and the latter depends on the device's channel width W.

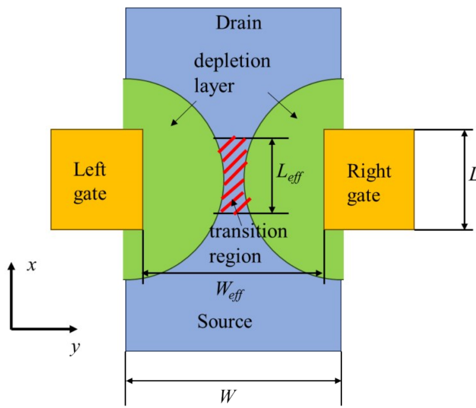

Fig. 3 Schematic diagram of the EdgeFET structure. The green area represents the depletion region formed after applying the gate bias voltage. (The actual channel width is W, effective channel width is W_{eff}, actual gate length is L, and effective gate length is L_{eff})
图3 EdgeFET的结构示意图,绿色区域为栅极施加偏压后产生的耗尽区(实际沟道宽度为W,有效沟道宽度为Weff,实际栅长为L,有效栅长为Leff)

In practical devices, due to the gate length being at the 170 nm scale and constrained by fabrication processes, the depletion regions formed in the channel under dual-side-gate biasing exhibit a non-uniform distribution, as illustrated in Fig. 3. To address this, the effective gate length L_{eff} ($L_{eff} = \alpha L$, α is a constant serving as the correction factor.) is introduced to replace the real gate length L. Furthermore, considering the overlap between the gate and the mesa induced by fabrication constraints, the effective gate width W_{eff} ($W_{eff} = \beta W$, β is a constant serving as the correction factor.) between the two gates is reduced compared to the channel width W. By incorporating L_{eff} and W_{eff} into Equation (13), the modified resonant frequency equation can be derived:

$$f = \frac{1}{4L_{eff}}\sqrt{\frac{\pi\hbar^2}{qm_n^{\ 2}}\left(qn_{s,0} + \frac{16\varepsilon V}{\pi W_{eff}}\right)} = \frac{1}{4\alpha L}\sqrt{\frac{\pi\hbar^2}{qm_n^{\ 2}}\left(qn_{s,0} + \frac{16\varepsilon V}{\pi\beta W}\right)} \quad , \quad (14)$$

2 Detector fabrication and experimental implementations

To validate the theory, a GaN/AlGaN EdgeFET THz detector with a gate length (L) of 170 nm and a gate width (W) of 200 nm is fabricated. Furthermore, a bow-tie-shaped planar integrated antenna with a radius of 90 μm is designed to improve the THz wave absorption efficiency. The bow-tie antenna offers advantages such as broad bandwidth, structural simplicity, and ease of fabrication[25]. Compared with devices without an antenna[26-27], integrating a bow-tie antenna significantly improves the coupling efficiency of terahertz energy and enhances device responsivity[28-29].

The devices are manufactured on a commercial GaN wafer with a substrate of 430 μm sapphire. The epitaxial junction comprises a 2 μm GaN layer and a 21 nm AlGaN barrier layer. The 2DEG offers an electron density of $n_0 = 5.12\times10^{12}$ and an electron mobility of $\mu = 2317$ $cm^2/V\cdot s$ at 300 K. To separate devices and evaluate the structures, the mesas of the HEMT are etched down to 150 nm.

The main problem in EdgeFET fabrication is to make both side gates have good contact with the mesa while avoiding excessive overlap. The mesa edges must be as smooth and steep as possible. The mesa fabricated by the ICP etching with an Al_2O_3 mask combined with electron beam lithography (EBL) and Lift-off technology has good etching morphology and a smooth, steep side wall. The mesa fabrication process is illustrated in Fig. 4(a)-(e). First, the sample is cleaned. Then, the mask pattern is transferred using EBL, followed by the deposition of a 90 nm Al_2O_3 film. A lift-off process is subsequently employed to remove the excess Al_2O_3, forming the final mask pattern. Finally, ICP etching is performed to form the mesa structure. This process reduces etching-related defects, making the deposited metal gate adhere closely to the side wall and enhancing device performance. Fig. 4(f)-(h) illustrate the following processes of fabrication of source, drain, antenna, electrode pads, and gate. Fig. 5(a) shows mesas fabricated based on this improved process.

The ohmic contacts comprised the Ti/Al/Ni/Au (20/120/55/45 nm) metal stacks and were rapidly annealed at 400 °C/700 °C/870 °C for 180 s/40 s/30 s in N_2. Ni/Au (20/200 nm) directly deposited all the metal pads, wires, and antennas. Fig. 5(b) shows the SEM images of the EdgeFET. The two arms of the antenna are connected to the gate and source of the device, respectively.

EBL is employed for gate fabrication to mitigate the overlap between the gate and mesa. Fig. 5(c) shows an SEM image of the side gate. The overlap is less than 20 nm.

The setup for characterizing the device is shown in Fig. 6(a), where the THz radiation from a BWO is chopped, collected, collimated and focused onto the detector located in a liquid nitrogen dewar, as illustrated in Fig. 6(b)(c). As the detector is insensitive to visible light, a Polymethylpentene (TPX) disk is used as the

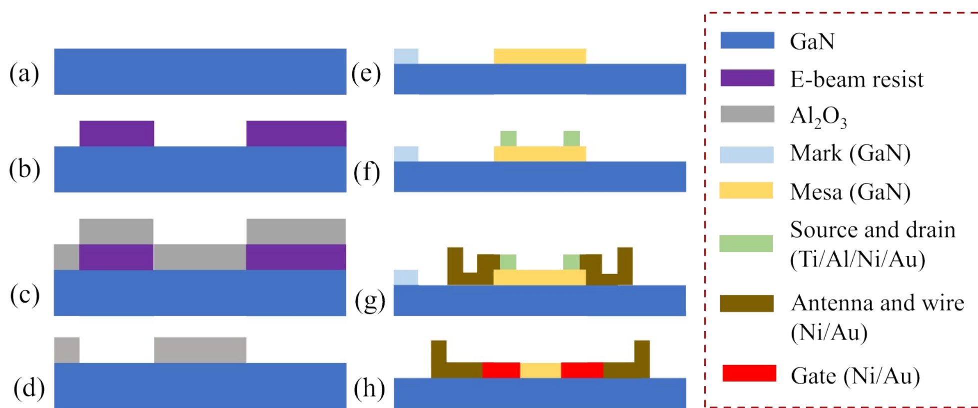

Fig. 4　The process flow chart of EdgeFET. (a) Wafer cleaning; (b) EBL pattern transfer; (c) Deposition of 90 nm Al_2O_3; (d) Lift-off to form the mask pattern; (e) ICP etching to define the mesa structure; (f) Fabrication of Ohmic source/drain electrodes; (g) Fabrication of metal antennas and wires; (h) Fabrication of metal gates. (a)-(g) is longitudinal section view of device; (h) is cross-sectional view of device

图 4　EdgeFET的工艺流程图。(a) 晶圆清洗;(b) EBL图形转移;(c) 90nm Al_2O_3沉积;(d) 剥离,形成掩模图形;(e) ICP蚀刻台面;(f) 制备欧姆接触源漏电极;(g)制备金属天线和导线;(h)制造金属栅极。(a)-(g)是器件的纵向剖面图;(h)是器件的横向剖面图

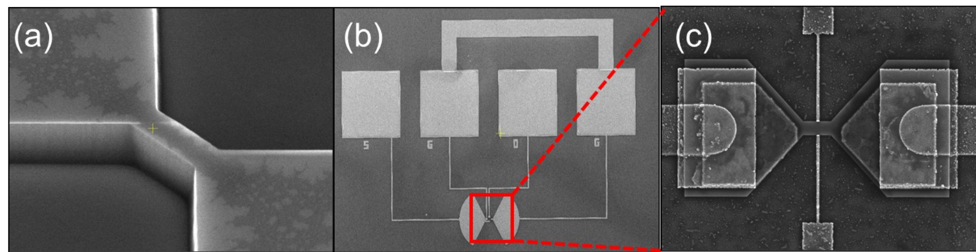

Fig. 5　(a) The mesa fabricated via a dry etching process using an Al_2O_3 mask, with EBL and lift-off; (b) EdgeFET containing a bow-tie antenna and electrodes; (c) SEM image of the side gate

图 5　(a)采用Al2O3作掩膜进行干法蚀刻,结合EBL和lift-off工艺制备的台面;(b)包含蝶形天线和电极的EdgeFET;(c)侧栅的SEM图片

window. The terahertz properties are studied using BWO operating at 200-384 GHz. A gate bias is applied to the device using a DC source, while the source-drain bias voltage is fixed at 0 V. The terahertz response signal from the detector is amplified by a lock-in amplifier.

3　Results and discussions

The device's DC and terahertz characteristics are measured at 300 K. Fig. 7(a)(b)(c) depicts the EdgeFET's DC characteristics. Fig. 7(d) describes at 300 K terahertz response of the EdgeFET versus gate voltage at 367 GHz. As shown in Fig. 7(d), only non-resonant responses occur at room temperature.

At 77 K, the EdgeFET is characterized using a backward wave oscillator (BWO) operating between 200 and 384 GHz. Fig. 8(a) illustrates the device's responsivity versus gate voltage at 240 GHz, 259 GHz, 265.5 GHz, 271 GHz, and 276 GHz. The method for determining the effective area required for the calculation of *Rv* is based on the method of "Physical area" described in Ref[30]. Two distinct response peaks are observed: one remains consistently centered at -3.08 V, independent of the incident wave frequency; the other shifts with frequency. In traditional HEMT, terahertz non-resonant response peaks exhibit frequency-independent characteristics, whereas the resonant response demonstrates strong frequency dependence. By analogy, the response centered at -3.08 V and independent of the incident wave frequency is classified as a non-resonant response, whereas the frequency-shifting response is identified as resonant response. In Fig. 8(b), the data are normalized relative to the maximum value of the non-resonant response for consistent comparison. The proposed device exhibits a resonant response superior to that of previously reported devices, which exceeds the maximum non-resonant response at 4 of the 5 detection frequencies. The resonant responsivity reaches 3.7 times that of the maximum non-resonant responsivity at 259 GHz.

To validate Equation (14), the experimentally measured relationship between the resonant frequency and the gate voltage is fitted. In Fig. 8(c), the black squares denote the experimental data points across various frequencies, and the red solid line indicates the theoretical resonant frequency controlled by gate voltage, as described by Equation (14) ($\alpha = 0.35$, $\beta = 0.8$). The fitted parameters are shorter than the physical dimensions. This discrepancy arises from two primary factors: under dual-gate biasing conditions, the non-uniform depletion region distribution in the channel results in an effective gate length that is smaller than the physical gate

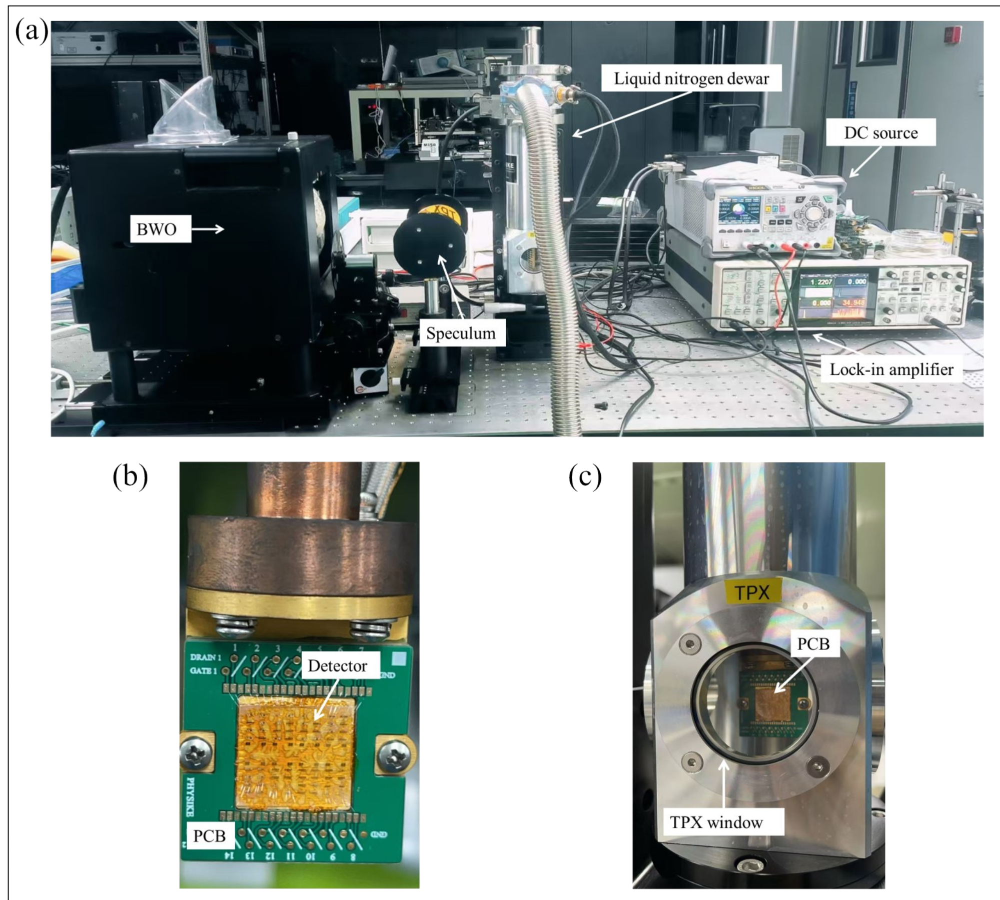

Fig. 6 (a) Image of terahertz detection platform; (b) Image of PCB; (c) Image of the liquid nitrogen dewar
图6 (a)太赫兹测试平台的图片;(b)PCB的图片;(c)液氮杜瓦瓶的图片

length, and process-induced overlap between the gate electrodes and the platform leads to an effective channel width that is narrower than the designed width. The theoretical curve is completely in line with the experimental data, demonstrating that the resonant frequency of the EdgeFET adheres to the relationship described by Equation (14), preliminarily validating the theory.

At 77 K, distinct resonant detection characteristics were successfully observed. Similar to the traditional HEMT, the EdgeFET demonstrates that its terahertz non-resonant response peaks exhibit frequency-independent characteristics, whereas the resonant response demonstrates strong frequency dependence. In the experiments, the resonant responsivities at 4 frequencies are higher than their corresponding non-resonant responsivities. However, at 265.5 GHz, the resonant responsivity is lower than the non-resonant responsivity. The variation in the relative intensity between resonant and non-resonant responses may result from antenna coupling and substrate effects[25,31-32], which needs further investigation in the future. Furthermore, the resonant detection response peaks of the EdgeFET exhibited a certain degree of broadening, and the responsivity remained relatively low. This may be attributed to losses present in the actual device.

Resonant detection has been reported in previous studies[13-16,33-38]. However, in those works, the resonant response voltage was extremely weak—often nearly undetectable, and significantly lower than the corresponding non-resonant response. Moreover, most of the previous studies did not provide quantitative responsivity values. In contrast, EdgeFET of this work exhibits a distinct resonant responses at 77 K, with a relatively high responsivity, achieving a resonant response that exceeds the non-resonant response. Consequently, the device demonstrates superior resonant performance compared to previously reported counterparts.

In addition, the effective gate length L_{eff} was significantly shorter than the actual gate length L. This discrepancy may stem from the simplified assumptions in the theoretical derivation, which neglect the carrier concentration gradient in the vertical current direction and approximate the current in the channel as one-dimensional.

To address these issues, the next phase of research will focus on developing a two-dimensional plasma wave propagation model to refine the theoretical framework of EdgeFET resonant detection. Furthermore, optimizing the device fabrication and structural design will enhance resonant detection responsivity to satisfy the sensitivity requirements of commercial terahertz detection systems.

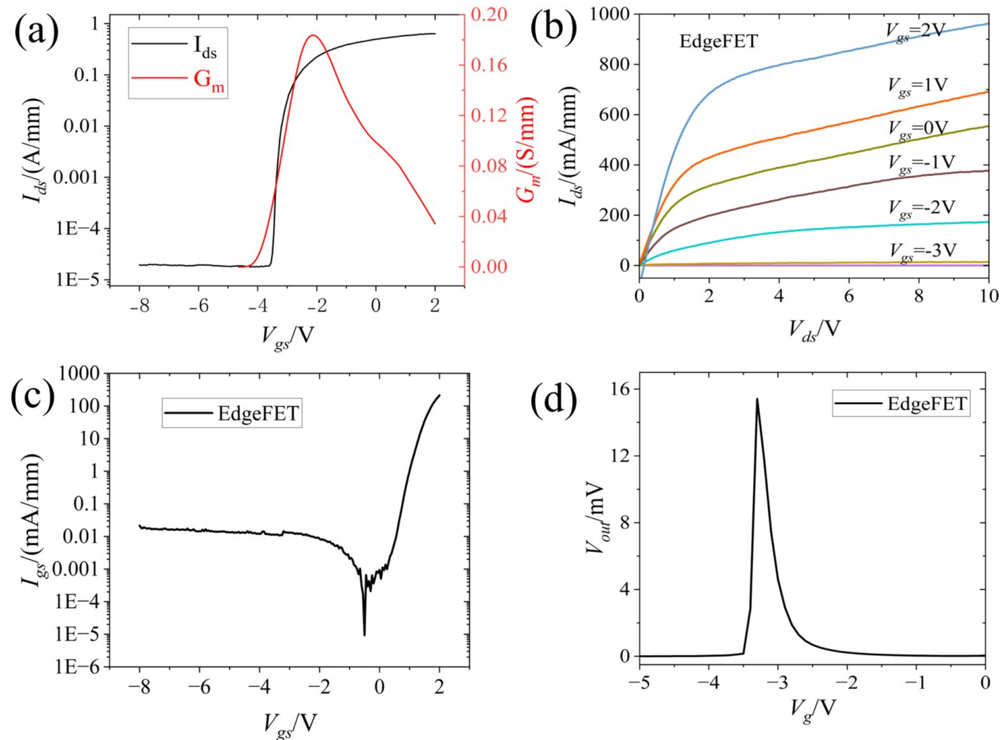

Fig. 7　At 300 K, the EdgeFET's (a) transfer characteristic curve under V_{ds} = 7 V (Threshold voltage V_{th} = -3. 55 V); (b) output characteristic curves; (c) leakage current curve; (d) At 367 GHz, THz response versus the gate voltage
图 7　在 300 K 下，EdgeFET 的(a)Vds = 7 V 时的转移特性曲线(阈值电压 Vth = -3. 55 V);(b)输出特性曲线;(c)漏电流曲线;(d)在 367 GHz 下太赫兹响应与栅压的关系曲线

4 Conclusions

In summary, this study presented theoretical research on the resonant detection of EdgeFET THz detectors and established a frequency model for resonant detection tailored to EdgeFET. An EdgeFET THz detector was fabricated with a gate length of 170 nm and a gate width of 200 nm, which was integrated with a bowtie antenna. The mesa was dry-etched with an Al_2O_3 mask to make good contact between the side gates and the mesa. Characterization in the 200 - 384 GHz range at 77 K revealed distinct resonant responses. The established device provided resonant responses higher than previously reported works, surpassing the maximum non-resonant response at the same frequency. The resonant responsivity at 259 GHz reached 3. 7 times the maximum non-resonant one. The accuracy of the EdgeFET resonant detection frequency model was preliminarily validated by fitting the experimental data on the relationship between resonant frequency and gate voltage with the theoretical model. This work lays a solid foundation for constructing higher-performance terahertz resonant detectors.

Reference

[1] Brinkmann S, Vieweg N, Gärtner G, et al. Towards quality control in pharmaceutical packaging: Screening folded boxes for package inserts[C]//2016 41st International Conference on Infrared, Millimeter, and Terahertz waves (IRMMW-THz). Copenhagen, Denmark, 2016: 1-2.

[2] Suen J Y. Terabit-per-Second Satellite Links: a Path Toward Ubiquitous Terahertz Communication[J]. Journal of Infrared, Millimeter, and Terahertz Waves, 2016, 37(7): 615-639.

[3] Saeedkia D. Handbook of terahertz technology for imaging, sensing and communications[C]//Physics, Engineering, Materials Science. Woodhead Publishing Limited, 2013.

[4] Jepsen P u., Cooke D g., Koch M. Terahertz spectroscopy and imaging – Modern techniques and applications[J]. Laser & Photonics Reviews, 2011, 5(1): 124-166.

[5] Lu J Q, Shur M S, Weikle R, et al. Detection of microwave radiation by electronic fluid in AlGaN/GaN heterostructure field effect transistors[C]//1997 Proceedings IEEE/Cornell Conference on Advanced Concepts in High Speed Semiconductor Devices and Circuits. Ithaca, New York, 1997: 211-217.

[6] Weikle R M, Lu J Q, Shur M, et al. Detection of microwave radiation by electronic fluid in high electron mobility transistors [J]. Electronics Letters, 1996, 32: 2148-2149.

[7] Lu J Q, Shur M S, Hesler J L, et al. Terahertz detector utilizing two-dimensional electronic fluid[J]. IEEE Electron Device Letters, 1998, 19(10): 373-375.

[8] Lu J Q, Shur M. Terahertz detection by high-electron-mobility transistor: Enhancement by drain bias[J]. Applied Physics Letters, 2001, 78: 2587-2588.

[9] Dyakonov M, Shur M. Shallow water analogy for a ballistic field effect transistor: New mechanism of plasma wave generation by dc current[J]. Physical Review Letters, 1993, 71(15): 2465-2468.

[10] Dyakonov M, Shur M. Detection, mixing, and frequency multiplication of terahertz radiation by two-dimensional electronic fluid[J]. IEEE Transactions on Electron Devices, 1996, 43(3): 380-387.

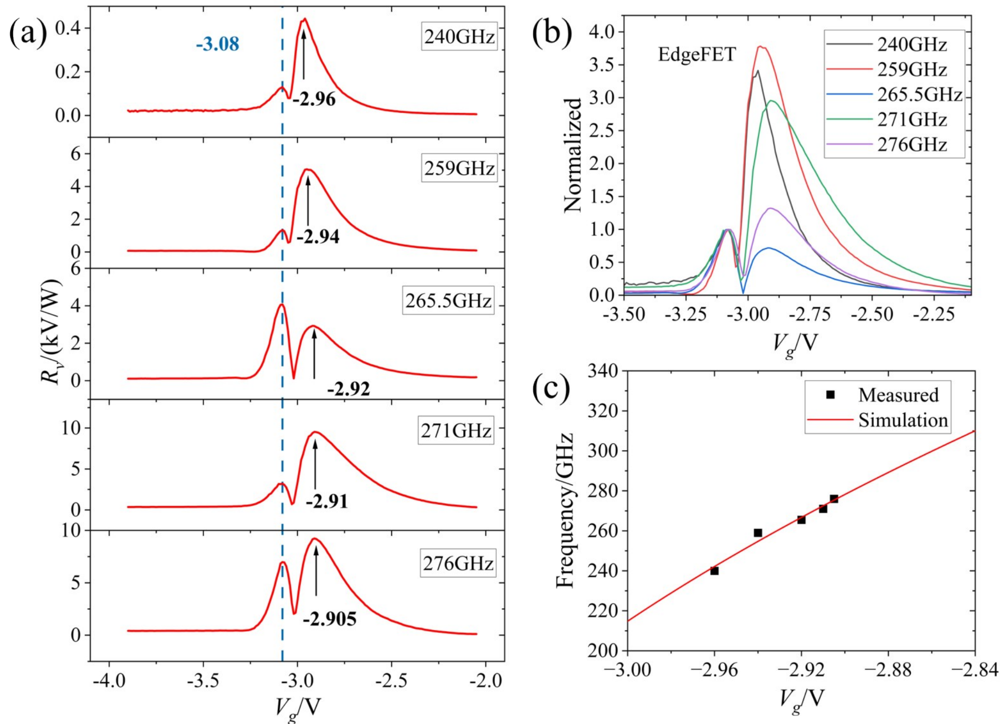

Fig. 8 (a) Under V_{ds} = 0 V, the R_v variations with gate voltage at 77 K at 240 GHz, 259 GHz, 265. 5 GHz, 271 GHz, and 276 GHz (The blue dashed line indicates the maximum non-resonant response for various frequencies at V_g = −3. 08 V); (b) The normalized non-resonant response; (c) The relationship between resonant frequency and gate voltage. The black squares indicate the gate voltage values at the center of the resonant response peak at 240 GHz, 259 GHz, 265. 5 GHz, 271 GHz, and 276 GHz, respectively. The red solid line indicates the resonance frequencies controlled by the gate voltage derived from Equation (14). : (L = 170 nm, W = 200 nm, α = 0.35, β = 0.8, $\varepsilon = 8.9\varepsilon_0$, $\varepsilon_0 = 8.854\times10^{-12}$ F/m, $\hbar$= 1.054×10^{-34} J·s, $q = 1.602\times10^{-19}$ C, $m_n = 0.2m_0$, $m_0 = 9.108\times10^{-31}$ kg, $n_{s,0} = 5.12\times10^{12}$ cm^{-2}) (Hall effect measurements be used to evaluate the $n_{s,0}$)

图8 (a)Vds = 0 V时,在77 K,240 GHz、259 GHz、265. 5 GHz、271 GHz和276 GHz频率下,Rv随栅极电压的变化(蓝色虚线表示在Vg = −3. 08 V时各频率下的最大非共振响应);(b)归一化非共振响应;(c)共振频率随栅压的变化关系。黑色方块分别表示240 GHz、259 GHz、265. 5 GHz、271 GHz和276 GHz频率下共振响应峰中心处的栅极电压值。红色实线表示由式(14)导出的栅电压控制的共振频率曲线。:(L = 170 nm, W = 200 nm, α = 0.35, β = 0.8, $\varepsilon = 8.9\varepsilon_0$, $\varepsilon_0 = 8.854\times10^{-12}$ F/m, $\hbar$= 1.054×10^{-34} J·s, $q = 1.602\times10^{-19}$ C, $m_n = 0.2m_0$, $m_0 = 9.108\times10^{-31}$ kg, $n_{s,0} = 5.12\times10^{12}$ cm^{-2})($n_{s,0}$由霍尔效应测量进行评估)

[11] Knap W, Kachorovskii V Y, Deng Y, et al. Nonresonant Detection of Terahertz Radiation in Field Effect Transistors[J]. Journal of Applied Physics, 2002, 91: 9346-9353.

[12] Dyakonov M I. Generation and detection of Terahertz radiation by field effect transistors[J]. Comptes Rendus Physique, 2010, 11(7): 413-420.

[13] El Fatimy A, Teppe F, Dyakonova N, et al. Resonant and voltage-tunable terahertz detection in InGaAs/InP nanometer transistors[J]. Applied Physics Letters, 2006, 89(13): 131926.

[14] Fatimy A E, Tombet S B, Teppe F, et al. Terahertz detection by GaN/AlGaN transistors[J]. Electronics Letters, 2006, 42(23): 1342-1344.

[15] Knap W, Deng Y, Rumyantsev S, et al. Resonant detection of subterahertz and terahertz radiation by plasma waves in submicron field-effect transistors[J]. Applied Physics Letters, 2002, 81(24): 4637-4639.

[16] Knap W, Deng Y, Rumyantsev S, et al. Resonant detection of subterahertz radiation by plasma waves in a submicron field-effect transistor[J]. Applied Physics Letters, 2002, 80(18): 3433-3435.

[17] Knap W, Teppe F, Dyakonova N, et al. Plasma wave oscillations in nanometer field effect transistors for terahertz detection and emission[J]. Journal of Physics: Condensed Matter, 2008, 20(38): 384205.

[18] Dyakonov M I. Boundary instability of a two-dimensional electron fluid[J]. Semiconductors, 2008, 42(8): 984-988.

[19] Popov V V. Suppression of the intermode plasmon scattering due to total internal reflection of oblique plasmons in a multichannel high-electron-mobility transistor[J]. Applied Physics Letters, 2008, 93(8): 083501.

[20] Cywiński G, Yahniuk I, Kruszewski P, et al. Electrically controlled wire-channel GaN/AlGaN transistor for terahertz plasma applications[J]. Applied Physics Letters, 2018, 112(13): 133502.

[21] Knap W, Marczewski J, Zaborowski M, et al. Field Effect Transistors Based Terahertz Detectors 25 Years History, State of the Art and Future Directions[C]//2018 43rd International Conference on Infrared, Millimeter, and Terahertz Waves (IRMMW-THz). 2018: 1-3.

[22] Kang Y, Dong H, Liu J, et al. The physical model, structural fabrication, and DC testing of lateral gate transistor terahertz detectors[J]. Journal of Infrared and Millimeter Waves, 2024, 43(4): 526-532.

[23] Gelmont B, Shur M, Moglestue C. Theory of junction between two-dimensional electron gas and p-type semiconductor[J]. IEEE Transactions on Electron Devices, 1992, 39(5): 1216-1222.

[24] Petrosian S, Shik A. Contact phenomena in low-dimensional electron systems[J]. Zhurnal Eksperimental noi i Teoreticheskoi Fiziki, 1989, 96: 2229-2239.

[25] Wang Xiaodong, Yan Wei, Li Zhaofeng, et al. Application of planar antenna in field-effect transistor terahertz detectors [J]. Chinese Optics, 2020, 13(1): 1-13.

[26] Lisauskas A, Spiegel W, Boubanga-Tombet S, et al. Terahertz imaging with GaAs field-effect transistors [J]. Electronics Letters, 2008, 44(6): 408-409.

[27] Nadar S, Videlier H, Coquillat D, et al. Room temperature imaging at 1.63 and 2.54 THz with field effect transistor detectors [J]. Journal of Applied Physics - J APPL PHYS, 2010, 108 (5): 054508.

[28] Öjefors E, Baktash N, Zhao Y, et al. Terahertz imaging detectors in a 65-nm CMOS SOI technology [C]//2010 Proceedings of ESSCIRC. 2010: 486-489.

[29] Hadi R A, Sherry H, Grzyb J, et al. A broadband 0.6 to 1 THz CMOS imaging detector with an integrated lens [C]//2011 IEEE MTT-S International Microwave Symposium. 2011: 1-4.

[30] Javadi E, But D B, Ikamas K, et al. Sensitivity of Field-Effect Transistor-Based Terahertz Detectors [J]. SENSORS, 2021, 21(9): 2909.

[31] Quarta G, Perenzoni M, D'Amico S. Co-Design and Optimization of a 320 GHz On-Chip Antenna for THz detection in 65nm CMOS Technology [C]//2021 International Conference on IC Design and Technology (ICICDT). 2021: 1-4.

[32] Perenzoni M, Cavallo D. Design of an efficient 900 GHz antenna in standard CMOS technology for imaging arrays [C]//2015 9th European Conference on Antennas and Propagation (EuCAP). 2015: 1-2.

[33] Sun J D, Qin H, Lewis R A, et al. The effect of symmetry on resonant and nonresonant photoresponses in a field-effect terahertz detector [J]. Applied Physics Letters, 2015, 106 (3): 031119.

[34] Otsuji T, Hanabe M, Ogawara O. Terahertz plasma wave resonance of two-dimensional electrons in InGaP/InGaAs/GaAs high-electron-mobility transistors [J]. Applied Physics Letters, 2004, 85(11): 2119-2121.

[35] Teppe F, Knap W, Veksler D, et al. Room-temperature plasma waves resonant detection of sub-terahertz radiation by nanometer field-effect transistor [J]. Applied Physics Letters, 2005, 87(5): 052107.

[36] Torres J, Nouvel P, Akwoue-Ondo A, et al. Tunable plasma wave resonant detection of optical beating in high electron mobility transistor [J]. Applied Physics Letters, 2006, 89 (20): 201101.

[37] Knap W, El Fatimy A, Torres J, et al. Plasma wave resonant detection of terahertz radiations by nanometric transistors [J]. Low Temperature Physics, 2007, 33(2): 291-294.

[38] Meziani Y M, Velázquez-Pérez J E, Coquillat D, et al. Terahertz detection using Si-SiGe MODFETs [C]//2013 Spanish Conference on Electron Devices. 2013: 167-170.

基于侧栅 AlGaN/GaN HEMT 的共振探测太赫兹探测器

靳晨阳[1,3,4,5], 康亚茹[1,5], 李叶然[1,3,6], 颜 伟[1,3*], 宁 瑾[1,3,4,5], 赵永梅[1,3,4,5], 李兆峰[1,2,3,4,5*], 杨富华[1,2,3], 王晓东[1,2,3,5]

(1. 中国科学院半导体研究所 半导体集成技术工程研究中心,北京 100083
2. 中国科学院大学 材料科学与光电研究中心,北京 100049
3. 中国科学院大学 材料科学与光电技术学院,北京 100049
4. 中国科学院大学 电子电气与通信工程学院,北京 100049
5. 中国科学院大学 集成电路学院,北京 100049
6. 怀柔实验室,北京 101499)

摘要:高电子迁移率晶体管(HEMT)太赫兹探测器由于栅宽过大,会导致沟道中产生杂散等离子体波模式,造成共振探测响应信号微弱,以及响应峰展宽。针对上述问题,提出一种侧栅 HEMT(EdgeFET)结构。基于传统 HEMT 的二维电子气(2DEG)流体动力学方程,建立了侧栅器件的共振探测模型。制备了侧栅 HEMT 探测器,并在 77 K 下进行了太赫兹共振探测实验。实验结果表明:EdgeFET 在 77 K 下展现出明显的共振响应,共振响应度可达到最大非共振响应度的 3.7 倍。实验数据与理论模型拟合良好,验证了模型的准确性。实验结果充分证实了侧栅 HEMT 在提升探测器共振性能方面的有效性,为开发下一代高性能太赫兹探测器提供了新的技术途径。

关 键 词:AlGaN/GaN HEMT;侧栅;太赫兹;共振探测

中图分类号:TN386 **文献标识码**:A